Energy Engineering

Tech Science Press

https://doi.org/10.32604/ee.2026.078440

ARTICLE

Low-Voltage PV-Storage DC System Protection via Dynamic Threshold Optimization

Zhukui Tan[1], Xiaoyong Cao[2,*], Qihui Feng[1], Dong Liu[2], Xiayu Chen[3] and Fei Chen[2]

[1]Electric Power Research Institute of Guizhou Power Grid Co., Ltd., Guiyang, China
[2]School of Electrical Engineering, Shanghai Jiao Tong University, Shanghai, China
[3]Guizhou Electric Power Construction Supervision & Consulting Co., Ltd., Guiyang, China

*Corresponding Author: Xiaoyong Cao. Email: xiaoyong.cao@sjtu.edu.cn

Received: 31 December 2025; Accepted: 24 February 2026; Published: 27 April 2026

ABSTRACT: The rapid integration of photovoltaic (PV) generation and energy storage systems has significantly increased the operational complexity of low-voltage direct current (LVDC) distribution networks in zero-carbon parks. Under highly variable operating conditions, conventional DC protection schemes relying on fixed overcurrent thresholds often suffer from maloperation or failure to trip, particularly during fluctuations in PV power, load switching, and changes in network topology. To address these challenges, this paper proposes an adaptive DC protection strategy based on an artificial neural network (ANN)-driven dynamic threshold optimization mechanism. The proposed method replaces static protection settings with an adaptive threshold that is continuously updated according to real-time system operating conditions. A dual-layer ANN architecture is developed to capture the nonlinear relationship between grid parameter variations and optimal protection thresholds. To enhance learning accuracy and convergence performance, the backpropagation neural network is further optimized using an improved grey wolf optimizer with a nonlinear convergence factor and mutation operator. The optimized ANN enables rapid and reliable threshold adjustment without relying on high-speed communication, making the scheme suitable for decentralized and edge-computing-based protection architectures. A comprehensive simulation platform for a PV-energy storage LVDC distribution system is established in MATLAB/Simulink to generate training and testing datasets under diverse scenarios, including variations in PV output, load shedding, different fault types, and measurement uncertainties. Simulation results demonstrate that the proposed adaptive protection strategy effectively eliminates threshold mismatch problems observed in fixed-setting methods. The results confirm that the proposed ANN-based adaptive protection strategy provides a robust, fast, and communication-independent solution for reliable protection of LVDC distribution networks with high penetration of renewable energy sources.

KEYWORDS: DC system; overcurrent protection; threshold setting; neural networks

1 Introduction

The development of zero-carbon parks is of great significance for advancing their high-quality growth. As a key practical scenario for achieving the “dual carbon” targets, their energy systems are highly reliant on distributed PV, energy storage, and diverse DC loads, which inherently creates a complex DC distribution environment. Zero-carbon parks are poised to play a pivotal role in ensuring rational energy consumption for high-quality development, reducing energy and resource consumption, and establishing a hub for green and low-carbon advancement, thereby contributing significantly to the goal of reducing carbon emission intensity [1].

Building on this foundation, the photovoltaic-energy storage DC building electrical system utilizes renewable energy to efficiently supply internal electrical loads. It adopts DC distribution technology to dynamically balance PV power generation, energy storage, and loads, while flexibly interacting with the grid to optimize power supply and consumption [2]. By converting building equipment into DC loads directly connected to the DC bus, the system improves energy efficiency and minimizes the conversion losses common in traditional AC systems. Furthermore, it supports the integration of distributed energy resources (DERs), prioritizing local consumption of PV-generated power, such as Building-Integrated Photovoltaics (BIPV), which embeds the PV system into the building structure to enable self-consumption and feed-in of surplus power to the grid [3].

With the proliferation of distributed energy resources and evolving load structures, the inherent DC characteristics of power sources, loads, and energy storage have become increasingly prominent. To ensure power quality and seamless integration of distributed energy, reliable protection for low-voltage direct current (LVDC) distribution systems is crucial [4]. LVDC relay protection involves line protection, insulation monitoring, and ground fault detection. However, the high-magnitude fault currents and rapid transient processes in LVDC grids pose significant detection challenges, necessitating adaptive threshold adjustments to maintain system stability and prevent cascading failures [5,6].

Previous studies have advanced the development of LVDC protection schemes. Existing research has analyzed primary and backup protection in AC grids, highlighting the trade-offs between sensitivity, speed, and selectivity for distance protection in AC-DC hybrid systems [7,8]. For LVDC microgrids with multiple distributed generators (DGs), an enhanced differential protection scheme achieved high-precision fault detection, while a centralized protection scheme based on post-transient derivatives addressed the selectivity limitations of voltage and current protection. Artificial Neural Networks (ANNs), owing to their pattern recognition capabilities, have been applied in protection systems, such as in methods that combine the Fast Fourier Transform (FFT) with ANNs to enhance fault detection. However, these methods often rely on preset, fixed thresholds, which diminishes their adaptability to varying grid conditions. Conventional LVDC fault detection typically sets one or more fixed current thresholds, tripping when the current exceeds a threshold for a specified duration [9,10]. This approach lacks the ability to finely distinguish transient characteristics and can lead to fault misclassification during heavy loading or operational mode changes. For example, fixed thresholds can lead to nuisance tripping or failure to trip during PV power fluctuations.

Furthermore, artificial intelligence (AI) technology, with its powerful self-learning, adaptive, and pattern recognition capabilities, offers innovative solutions for fault prediction and adaptive settings in distribution networks [11]. For instance, AI-based methods employ intelligent algorithms to learn from and train on fault data, thereby avoiding the tedious process of manual setting calculations and enabling fault diagnosis without predefined values [12]. Some researchers have proposed protection schemes based on fuzzy algorithms that utilize wavelet transforms and trained weights for fault discrimination. While these schemes have been practically validated, they exhibit poor tolerance to fault resistance [13]. Other research has utilized multiple neural networks for fault detection and localization; however, this approach involves complex fault feature extraction and demands a substantial training workload [14,15].

In LVDC systems with high photovoltaic PV penetration, line currents are no longer deterministic quantities dominated by a single source, but stochastic and time-varying processes jointly influenced by PV output fluctuations, energy storage states, load variations, and system control modes. Under changing operating conditions such as rapid PV power variations, sudden load shedding, or fault events, the transient characteristics of fault currents and non-fault operating currents may exhibit significant overlap in their statistical distributions, thereby violating the separability assumption underlying conventional fixed-threshold overcurrent protection [16]. As a result, operating current surges may trigger maloperation during

PV output increases, while suppressed fault currents under PV reduction or load shedding may lead to failure-to-trip. These phenomena indicate that protection misoperation and refusal in LVDC systems with high PV penetration are fundamentally caused by the time-varying and uncertain nature of current characteristics, highlighting the necessity for protection mechanisms capable of dynamically adapting threshold settings to real-time operating conditions.

The optimization of ANN parameters for fault thresholds is a non-convex problem with many local minima. Particle Swarm Optimization (PSO) is highly sensitive to the tuning of inertia weights and learning factors [17]. Improper tuning leads to rapid stagnation in local optima. Genetic Algorithms (GA) rely on complex selection, crossover, and mutation operations, which are computationally expensive and slow to converge, making them less suitable for offline training iterations where speed is a factor [18]. While Adam is excellent for deep learning gradient descent, GWO is less dependent on gradient continuity and better explores the global search space for the initial weight distribution, preventing the network from starting in a poor basin of attraction [19]. GWO employs a leadership-based hunting mechanism that naturally balances exploration and exploitation with fewer control parameters, offering superior convergence stability for this specific application.

In the context of real-time protection for power systems deployed on low-power edge devices, the selection of models must balance multiple constraints, including computational efficiency, memory footprint, inference latency, and output smoothness. SVM is typically used for offline fault classification where computational speed is secondary to margin maximization; however, its kernel-based inference leads to non-deterministic latency which is unacceptable for real-time protection loops [20]. Random Forest (RF) is often used in scenarios requiring high interpretability, but its memory-intensive ensemble structure and discontinuous step-function output generate threshold "jitter" that destabilizes protection logic [21]. LSTM is widely used in load forecasting where long-term temporal dependencies are critical; however, its sequential recurrent calculation introduces high latency, which fails to meet the sub-millisecond fault detection requirement of DC systems [22]. In contrast, the selected feedforward ANN provides a good balance between nonlinear mapping capability, computational efficiency, and ease of deployment. Its simple structure enables fast inference, stable performance, and deterministic execution, which are essential for protection-oriented applications.

To overcome these limitations, this study proposes a novel fault detection algorithm for LVDC grids based on dynamic threshold adjustment using an Artificial Neural Network (ANN). Compared with existing adaptive schemes, the core innovation of this paper lies in driving the real-time optimization of dynamic thresholds via an ANN, achieving a communication-independent protection mechanism based on an edge computing architecture, and effectively adapting to scenarios with PV output fluctuations. The key innovations are as follows:

A dual-layer ANN architecture is proposed to map grid parameters to optimal protection thresholds.

A localized, dynamic threshold update mechanism is designed, which operates without high-speed communication and leverages edge computing for rapid response.

The effectiveness and robustness of the proposed method are validated through extensive simulations under PV power fluctuations and load switching.

The remainder of this paper is structured as follows: Section 2 analyzes the fault characteristics of the LVDC system. Section 3 details the protection configuration and the proposed threshold optimization scheme. Section 4 presents the simulation results and validation. Finally, Section 5 concludes the study.

2 Fault Characteristics Analysis

2.1 Characteristics of DC Building Parks

The basic layout of a DC building park is illustrated in Fig. 1. When a fault occurs in a certain area of the park's power system, conventional AC grids, due to the difficulty in controlling fault currents and their reliance on synchronous interconnection, are prone to triggering cascading failures and may even lead to large-scale blackouts.

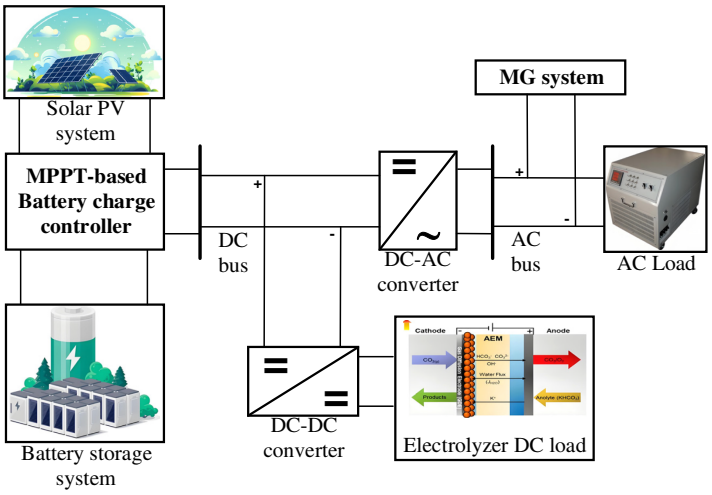

Figure 1: The layout of a DC building park.

In contrast, DC microgrids, by leveraging the intelligent isolation capabilities of power electronic converters and their distributed system architecture, can rapidly isolate the faulted area. This effectively contains fault propagation and significantly reduces the risk of system outage. Therefore, with its distinct advantages, including high efficiency, flexibility, strong compatibility, and low losses, DC technology demonstrates superior performance compared to traditional AC distribution systems and has become a key technology for various types of zero-carbon parks to achieve their carbon reduction targets.

2.2 Fault Analysis

Operational changes in LVDC networks, like variations in PV power generation or sudden load reductions, alter key system parameters such as impedance and damping characteristics. These alterations cause fault currents to become non-stationary, meaning they deviate from predictable patterns under steady-state conditions. As a result, fixed protection thresholds, which are calibrated based on nominal operations, often fail to adapt, leading to unreliable protection responses.

PV output variations, caused by factors such as passing clouds or changes in solar irradiance, significantly influence the network's equivalent impedance. When a fault occurs, the fault current superimposes with the stochastic current injected by PV units. If the PV output increases abruptly, the combined current may exceed the preset protection threshold, leading to nuisance tripping even in the absence of an actual fault. Conversely, a sudden decrease in PV generation can reduce the fault current magnitude below the threshold, resulting in a protection failure-to-trip.

Load-shedding events also considerably impact protection reliability. A sudden reduction in load alters the damping characteristics of the system, leading to a rapid decay of the fault current. If the protection threshold remains static, the falling current may drop below the trip setting, delaying or preventing fault

detection. This scenario underscores the necessity of a threshold adjustment mechanism that responds to load variations in real time.

For fault analysis, consider the LVDC distribution network structure shown in Fig. 2a, where L_d denotes the current-limiting inductor, K_s is the AC circuit breaker, K_0 to K_4 are DC circuit breakers, B_1 to B_2 are busbars, and F_1 and F_2 are feeder lines. Fault points f_1 and f_2 represent short-circuit faults on the feeder and busbar, respectively. Current flow is defined as positive from the busbar to the feeder, denoted by currents i_0 to i_4. The equivalent circuit for fault point f_1 is shown in Fig. 2b. Given the low voltage and short feeder distances in LVDC networks, distributed capacitance effects are negligible. Consequently, the passive nature of the load interface and negligible distributed capacitance imply that the fault current idc at f_1 is primarily supplied by downstream DGs or Energy Storage Systems (ESS).

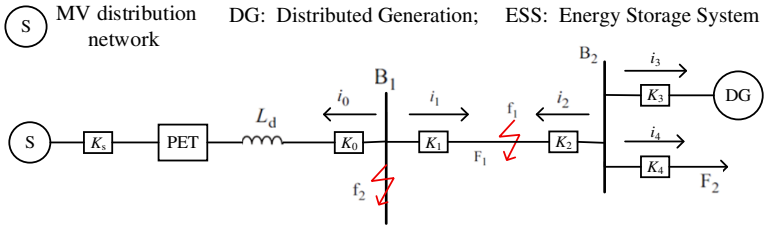

(a) LVDC Distribution network structure and fault illustration

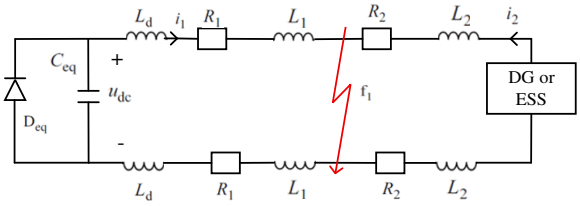

(b) Short-circuit fault equivalent circuit

Figure 2: Analysis of the LVDC power grid fault.

In Fig. 2b, R_1 and L_1 denote the equivalent resistance and inductance of feeder section F_1 from fault point f1 to the upstream busbar B1. Similarly, R_2 and L_2 represent the equivalent resistance and inductance of the downstream line from f_1. The equivalent diode D_{eq} models the unidirectional current flow at the load interface, while C_{eq} represents the equivalent capacitance of the power electronic transformer (PET) or related devices.

3 Configuration and Setting of Protection Devices

The protection scheme for a DC line bipolar short-circuit fault involves utilizing overcurrent protection to rapidly detect the occurrence of the fault. Additionally, the converters at both ends are locked out at the outlet, and the circuit breakers are coordinated to clear the fault current.

3.1 Analysis of Bipolar Short-Circuit Fault Characteristics

This paper focuses on the analysis of fault characteristics prior to the converter lockout, with the equivalent circuit shown in Fig. 3. Based on the characteristics of the LVDC interface and the operational characteristics of PET, the fault development during a short-circuit event in the LVDC distribution network can be divided into three stages: capacitor discharge, current decay, and stable output.

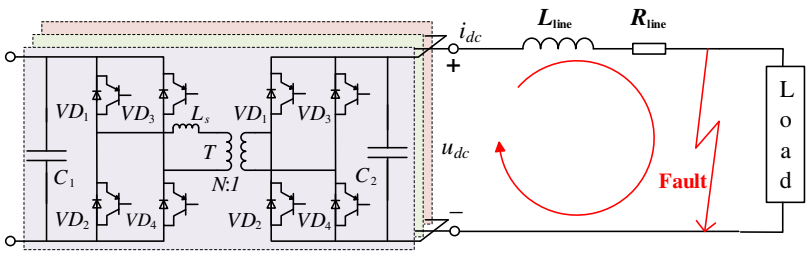

Figure 3: Schematic diagram of feeder short-circuit current.

During the capacitor discharge stage of the entire system, the DC voltage drops, and the current rises rapidly. In this stage, both the primary and secondary side capacitors of the DAB participate in the discharge. The loop current remains below the current limit, thus not posing an overcurrent threat to the PET. In the early fault stage, as shown in Figs. 2 and 3, the interface loop equation for this stage is:

$$LC\frac{d^2 i_{\mathrm{dc}}}{dt^2} + RC\frac{di_{\mathrm{dc}}}{dt} + i_{\mathrm{dc}} = 0 \tag{1}$$

In the equation, R, L, and C are obtained from the specific circuit parameters. The DC system generally satisfies the underdamped condition:

$$i_{dc} = \frac{U_0}{\omega L} e^{-\alpha t} \sin(\omega t) - \frac{I_0 \omega_0}{\omega} e^{-\alpha t} \sin(\omega t - \beta) \tag{2}$$

In the equation, U_0 represents the initial voltage value, I_0 represents the initial current value; $\alpha = \mathrm{R}/(2\mathrm{L})$, $\omega_0 = 1/\sqrt{\mathrm{LC}}$, $\omega^2 = \omega_0^2 - \alpha^2$, $\beta = \arctan(\omega/\alpha)$.

In the second stage of the fault, for other interfaces, the diode conduction resistance is neglected. The loop equation for this stage is:

$$L\frac{di_{dc}}{dt} + Ri_{dc} = 0 \tag{3}$$

Variations in DG output, such as those from PV systems, can significantly alter the network's equivalent impedance and damping characteristics, thereby affecting the parameters in the aforementioned equations and the behavior of fault currents. When PV output suddenly increases, the equivalent impedance decreases, leading to an increase in the magnitude of the fault current i_{dc} in Eq. (2). This may cause the fault current to exceed a fixed protection threshold, triggering a false trip even in the absence of an actual fault. Conversely, when PV output decreases, the equivalent impedance increases, resulting in a reduction in the magnitude of the fault current. In Eq. (2), i_{dc} may then fall below the threshold, leading to a failure-to-trip of the protection. Particularly during the current decay phase, changes in damping characteristics will accelerate the current decay, further elevating the risk of failure-to-trip.

The fault current for this stage can be expressed as:

$$i_{dc} = I_0' e^{-\frac{R}{L}t} \tag{4}$$

In this equation, I_0' represents the initial current at the second stage. During the second stage, the fault current gradually decays through the diode's freewheeling path.

When the current decays to the current limit command, the control system exits saturation and enters the third stage. Before the fault is cleared, the PET adjusts the terminal voltage, causing the output current to stabilize.

3.2 Protection Configuration and Protection Setting

As analyzed above, after the occurrence of a bipolar short-circuit fault, fault currents exist in both the DC line and the converter's bridge arms. To ensure the safety of the equipment, converters are typically equipped with bridge arm overcurrent protection in practical engineering applications. The overcurrent protection works in conjunction with the bridge arm overcurrent protection, where either criterion being satisfied will trigger a converter lockout signal to clear the fault current. The protection criterion is:

$$\begin{cases} \left|I_{d,p}\right| > I_{set,S} \cup \left|I_{d,n}\right| > I_{set,S} \\ I_{set,S} = K_I I_N \\ \Delta t \geq \Delta t_{set,OC} \end{cases} \tag{5}$$

In the equation, $I_{d,p}$ and $I_{d,n}$ represent the positive and negative DC line currents, respectively; $I_{set,S}$ is the current threshold value; K_I is the overcurrent criterion current coefficient; $\Delta t_{set,OC}$ is the duration of the overcurrent protection judgment; and I_N is the rated current of the converter's DC side.

To ensure the reliability of the protection action, the protection should perform continuous checks multiple times. The setting value for the duration of the judgment time depends on the number of continuous checks and the sampling frequency:

$$\Delta t_{set,LVOC} = \mathrm{n}T = \frac{n}{f} \tag{6}$$

In this equation, n is the number of continuous checks; T is the sampling period; and f is the sampling frequency.

For the overcurrent criterion, on one hand, it should cooperate with the neighboring lower-level DC line protection to prevent misoperation in the event of a fault in the lower-level line, thereby avoiding fault current from the next level. Due to the electrical isolation effect of the high-frequency transformer and the support from the converter's outlet capacitor, the DC/DC converter's low-voltage side protection experiences only minimal changes in the medium-voltage DC current before it acts. This is approximated as I_N in subsequent calculations.

On the other hand, it should cooperate with the converter's own protection. Under the most severe conditions, the overcurrent protection should act to lock out the converter before the bridge arm fault current reaches the set value for the bridge arm overcurrent protection. Specifically, the latest time t_2 for the overcurrent protection to operate before locking the converter should satisfy:

$$\max\left\{\left|\mathrm{i}_{p,m}\left(t_2\right)\right|, \left|\mathrm{i}_{n,m}\left(t_2\right)\right|\right\} = I_{set,oc,brg} \tag{7}$$

In this equation, $i_{p,m}$ and $i_{n,m}\,(m = a, b, c)$ represent the current for the upper and lower bridge arms of the three-phase converter, respectively, and $I_{set,oc,brg}$ is the set current value for the bridge arm overcurrent protection.

The fault current $i_{dc}\left(t_1\right)$ flowing through the protection point at time t_1 can be determined. Considering that the overcurrent protection may act before the bridge arm overcurrent protection, to ensure that the

converter equipment is not damaged before fault clearance, the current setting for the overcurrent protection should be smaller than the threshold for the protection:

$$I_{set,S} < i_{dc}(t_1) \tag{8}$$

The overcurrent criterion current coefficient should satisfy:

$$1 < K_I < \frac{i_{dc}(t_1)}{I_N} \tag{9}$$

3.3 Protection Threshold Optimization Scheme

Traditional current protection devices face new technical challenges: the probability of protection device failure-to-trip and maloperation increases, and protection sensitivity significantly decreases. These issues pose serious threats to the stability and safety of distribution networks. In contrast, adaptive current protection has advantages such as strong dynamic adaptability, high fault identification performance, good economy, and high protection reliability.

Fixed-threshold protection methods exhibit reliability issues under varying grid operating conditions. Under normal conditions, a fixed threshold can effectively distinguish between internal and external faults within the DC cable protection zone, as the significant difference between fault energy characteristics and the threshold ensures reliable protection decisions. However, during heavy loading or operational mode changes that lead to increased power transmission in the cable, the fixed threshold loses its adaptability. Test results indicate that in such scenarios, the minimum fault energy for some cable segments may fall below the preset threshold.

This can cause the protection system to misclassify an internal fault as an external fault or a no-fault condition, resulting in a protection failure-to-trip and delaying fault clearance.

To address this issue, this paper proposes a dynamic threshold optimization scheme based on an ANN. The scheme employs a dual-layer ANN architecture: the first layer maps the impact of grid parameter variations on voltage, while the second layer analyzes the voltage patterns to adaptively update the protection threshold. The choice of a two-layer ANN architecture is to achieve the best balance between nonlinear mapping capability and computational latency on edge devices. A single layer is often insufficient to capture the complex nonlinear relationships associated with high-impedance faults. Conversely, deep networks introduce excessive computational overhead, resulting in inference delays that exceed the strict 1–2 ms requirement for LVDC protection. The selection of 10 neurons in the hidden layer was determined through empirical ablation studies. When the number of neurons is increased beyond 10, the gain in accuracy diminishes, while the floating point operations increase linearly, thereby posing a risk of violating real-time performance constraints. The schematic of the BP neural network is shown in Fig. 4.

To enhance the generalization capability of the ANN and mitigate the risk of overfitting, a rigorously curated training dataset was developed to encompass a broad spectrum of operating conditions. During the training process, the MAE on the validation set was continuously monitored. An early stopping strategy was employed such that training was terminated once the validation error exhibited no significant reduction over a predefined number of consecutive epochs. This approach effectively prevents the model from continuing to learn idiosyncratic noise in the training data, thereby preserving its ability to generalize to unseen scenarios.

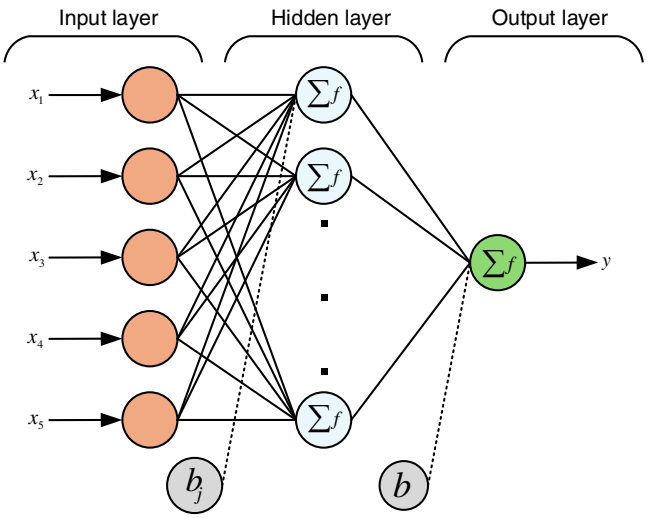

Figure 4: Neural network architecture schematic.

As BP neural networks rely on the gradient descent method, they are susceptible to getting trapped in local optima. The proposed Improved Grey Wolf Optimizer (IGWO) enhances global search capability and convergence speed through a nonlinear convergence factor and a mutation operator.

In the traditional GWO, the convergence factor a decreases linearly with the number of iterations:

$$a = 2 - \frac{2t}{t_{\max}} \tag{10}$$

This linear strategy is simple but lacks flexibility, making it unable to adapt to the search dynamics of complex optimization problems. IGWO introduces a non-linear convergence factor, employing a Sigmoid function to adjust the decreasing pattern of a. The Sigmoid function, with its smooth transition characteristics, can better balance exploration and exploitation. The improved formula for a is:

$$a = a_{\max} - \frac{1}{1 + \exp\left(-\frac{t}{t_{\max}}\right)} \tag{11}$$

The nonlinear convergence factor of the IGWO utilizes a Sigmoid function to adjust the decay pattern, offering three key advantages: it ensures a smooth transition between global exploration and local exploitation by maintaining a higher convergence factor in early iterations for extensive search space coverage, then gradually reducing it for refined optimization in later stages; it enhances population diversity and avoids premature convergence through an integrated mutation operator that introduces controlled perturbations, allowing the algorithm to escape local optima effectively; and it improves robustness and convergence speed in complex optimization scenarios, such as the ANN-based protection threshold setting discussed, by adaptively balancing exploration–exploitation dynamics without relying on sensitive parameter tuning. This mechanism is particularly beneficial for real-time applications like adaptive protection in LVDC grids, where rapid and reliable threshold adjustment is critical under varying operating conditions.

When dealing with multimodal or high-dimensional functions, traditional GWO is prone to losing population diversity, which leads to premature convergence. A mutation operator is introduced to simulate mutation in biological evolution, increasing population diversity and avoiding local optima.

The operation of the mutation operator is as follows: Let the current position vector of a wolf be $\vec{x} = (x_1, x_2, \ldots, x_n)$, where n is the dimension. Randomly select a dimension i $(1 \leq i \leq n)$ from the vector and mutate its value:

$$x_i' = x_i + \lambda q \tag{12}$$

In this equation, λ is a coefficient controlling the mutation strength, ranging from [−1, 1], a negative value indicates downward mutation, while a positive value indicates upward mutation. q is a random number generated within the neighborhood, typically based on the current value or the search space range.

The training process of the proposed improved BP neural network is illustrated in Fig. 5. To address the non-stationary nature of fault and non-fault current signals, the ANN does not directly use raw instantaneous currents. Instead, normalized and window-based statistical features, such as short-time RMS values, incremental changes, and relative deviation indices, are employed as inputs. To distinguish transient disturbances from actual faults, the ANN utilizes time-window-based features, such as short-duration RMS variation, sustained current deviation, voltage collapse indicators, and rate-of-change persistence. Transient disturbances such as inrush currents typically exhibit short duration and rapid self-recovery, whereas genuine faults result in sustained abnormal current and voltage behavior across multiple variables. These features effectively reduce sensitivity to absolute magnitude variations and operating point shifts. The occurrence time of non-fault events is first synchronized and used as a trigger for threshold adaptation. If the detected event is identified as a fault, no adjustment signal is generated, and consequently, the threshold remains unchanged. This design ensures that fault identification functionality remains unaffected by updates intended for non-fault scenarios, thereby preserving the reliability and stability of fault detection under varying operating conditions.

The threshold adjustment using the improved BP neural network is essentially a process of automatically optimizing network parameters through training. The neural network involves two learning phases: forward signal propagation and error backpropagation. During forward signal propagation, signals are input from the input layer, processed through the hidden layer, and reach the output layer. Through the error back-propagation algorithm, parameters are iteratively updated using the gradient descent method to minimize the prediction error. Time series prediction is based on an autoregressive model constructed from historical data, which posits that the current value is influenced by the previous n historical values. Data preprocessing is performed to remove missing values or outliers that significantly deviate from the normal range. The data is then linearly scaled to the [0, 1] interval using min-max normalization to eliminate the influence of dimensions.

The neural network adopts a three-layer structure. The input layer has 5 nodes, determined by the size of the time window. This implies that the time series prediction is based on an autoregressive model where the current value is influenced by the previous 5 historical values. The output layer consists of a single node, corresponding to the single-step prediction task of forecasting the value at the next time point. The hidden layer is configured as a single layer with 10 nodes, a structure that demonstrated optimal performance in the simulation experiments detailed in the following chapter.

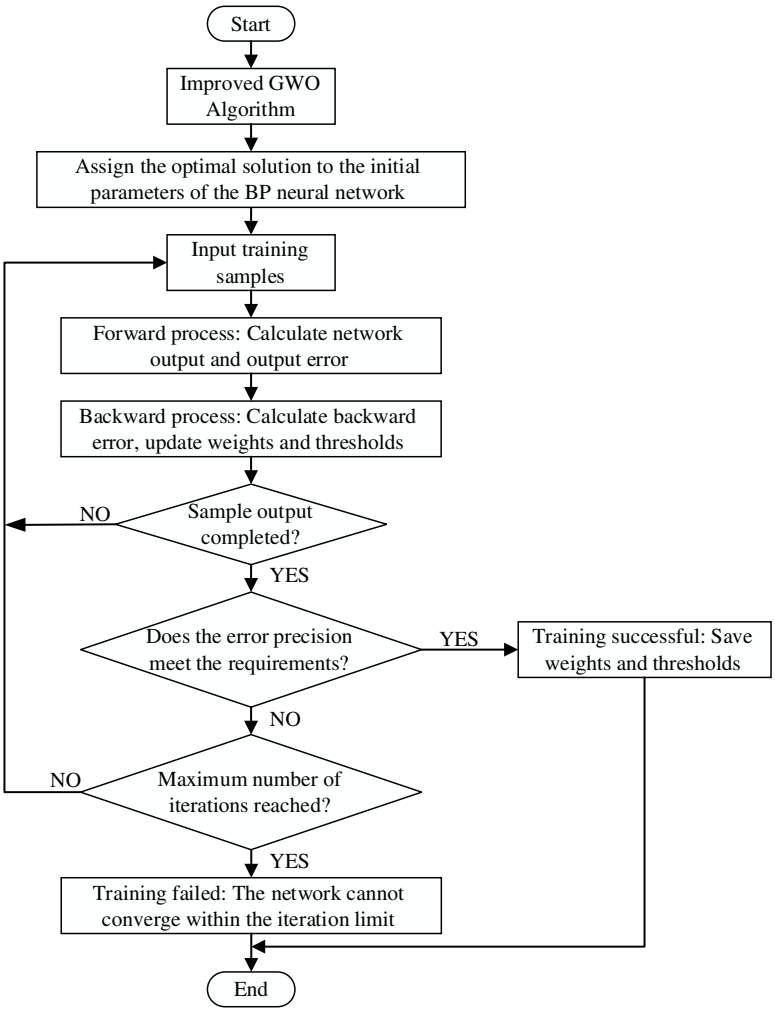

Figure 5: BP neural network training flowchart.

The weights of the network connections and their corresponding biases are updated based on the prediction error. To validate the reliability of the established neural network model, its results were compared with actual measured values using the Mean Absolute Error (MAE) statistical metric. Performance is evaluated by comparing predicted values y_{pred} with true values y_{true}:

$$MAE = \frac{1}{N}\sum_{i=1}^{N}\left|y_{pred}^{(i)} - y_{true}^{(i)}\right| \tag{13}$$

where *MAE* reflects the average magnitude of the deviations.

After the aforementioned improved BP neural network completes training and provides initial predictions y_{pred}, an optimization phase is introduced to further enhance prediction performance. This optimization model combines the neural network's prediction results with domain knowledge, physical constraints, or the statistical properties of the data itself.

The optimal threshold or decision boundary is determined via an expected loss minimization model, which transforms prediction information into an optimal setting value. The objective is to minimize the expected value of this loss function under the predicted current distribution:

$$E[L] = \int_{-\infty}^{I_{set}} c_1 (I_{set} - I) \Phi(I)\, dI + \int_{I_{set}}^{\infty} c_2 (I - I_{set}) \Phi(I)\, dI \tag{14}$$

where I_{set} is the setting value to be optimized, I is the random current variable, $\Phi(I)$ is the probability density function of the current, c_1 is the unit loss coefficient when $I < I_{set}$, and c_2 is the unit loss coefficient when $I > I_{set}$.

To solve for the optimal setting value, we differentiate the expected loss function with respect to I_{set}^* and set the derivative to zero. Applying the Leibniz integral rule:

$$\begin{cases} c_1 \int_{-\infty}^{I_{set}} \Phi(I)\, dI = c_1 F(I_{set}) \\ -c_2 \int_{I_{set}}^{\infty} \Phi(I)\, dI = -c_2 [1 - F(I_{set})] \end{cases} \tag{15}$$

Substituting this into the differentiated loss function and setting the derivative to zero yields:

$$c_1 F(I_{set}) - c_2 [1 - F(I_{set})] = 0 \tag{16}$$

The optimal setting value is obtained as:

$$I_{set}^* = F^{-1}\left(\frac{c_2}{c_1 + c_2}\right) \tag{17}$$

where F^{-1} is the inverse of the cumulative distribution function, the ratio $\frac{c_2}{c_1+c_2}$ represents a critical probability threshold that directly reflects the tolerance for the two types of risks. The optimal solution does not pursue absolute predictive accuracy but rather the most economical decision boundary that minimizes the overall expected loss during long-term operation.

The proposed enhanced BP neural network employs edge computing to process data and update thresholds locally, eliminating dependence on high-speed communication links. First, input data is organized by fault severity and labeled to form separate target vectors for fault and non-fault states. The updated threshold is then passed in real time to the Discrete Wavelet Transform module. The threshold update operates on a slower time scale than the fault detection logic. While the ANN updates the threshold at a 1 ms interval, the protection decision requires the fault current to continuously exceed the threshold over multiple sampling periods, as defined in Eq. (6). This time-scale separation prevents instantaneous threshold fluctuations from triggering protection oscillations. Second, the ANN output exhibits inherent smoothness due to its nonlinear regression nature and training under noisy and stochastic operating conditions. As a result, the generated thresholds vary gradually rather than abruptly, even under fast changes in input variables, which reduces the likelihood of threshold chattering.

4 Simulation and Validation

The proposed ANN-based protection scheme is designed with practical edge deployment in mind, and therefore imposes modest hardware requirements. In terms of computation, the online operation of the ANN only involves forward propagation, which consists of a limited number of multiplications and additions. This computation can be efficiently executed on commonly used edge devices such as industrial microcontrollers, DSPs, or embedded processors typically integrated in IEDs. The memory requirement is minimal, as only the trained network weights and biases need to be stored locally. Moreover, the scheme relies solely on locally measured current and voltage signals, requiring no additional sensing hardware or high-speed communication interfaces.

In the proposed edge-computing-based protection scheme, core protection logic and ANN inference run locally on the edge device, enabling real-time fault detection and tripping decisions independent of central controller communication—thus immune to external latency. The ANN is trained on data from a time window of 5 consecutive time points and updated every 1 ms. Simulations validating severe packet loss scenarios confirm that even with loss exceeding 10%, the system maintains stable threshold outputs without false trips, ensuring high robustness via a local sample-and-hold mechanism that preserves data integrity under adverse conditions.

To validate the effectiveness of the proposed algorithm, a power grid simulation model was developed in the MATLAB/Simulink environment. As shown in Fig. 6, the model features a DC bus as the core power hub. On the left side, two AC loads are connected in parallel to an AC source to simulate AC power consumption scenarios; the AC power is converted to DC power by an AC/DC converter and fed into the DC bus. On the right side of the DC bus, two types of source-storage modules are connected: an Energy Storage System (ESS) comprising a battery pack and a bidirectional DC/DC converter, and a PV generation unit integrated via a unidirectional DC/DC converter.

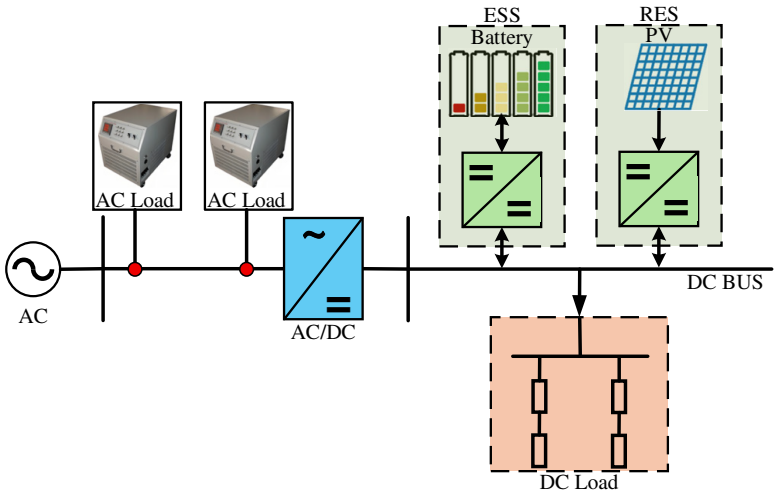

Figure 6: Simulation model structure schematic.

Additionally, a DC load is configured downstream of the DC bus to simulate the power demand on the DC side. All modules are coupled to the DC bus through power electronic conversion devices, providing a high-fidelity simulation environment for testing the LVDC grid algorithm.

To ensure the proposed ANN-based dynamic threshold method can generalize well across different operating scenarios, this study built a comprehensive training dataset covering various fault types, locations, and conditions. The data was generated from a simulation model of a PV-energy storage DC distribution system, covering multiple DC network fault scenarios, including bipolar short-circuit faults, unipolar positive/negative short-circuit faults, inter-line short circuits, high-impedance ground faults, and intermittent arcing fault.

For the generation of data under both normal and disturbed conditions, the simulation model simulated various operating states, including PV power output fluctuations, changes in the energy storage's State of Charge (SOC), different load levels, and disturbance scenarios such as load shedding and the connection of pulsed loads. Furthermore, measurement noise, electrical parameter deviations, and a stochastic PV disturbance model were randomly superimposed in the simulations to enhance the realism of the data,

enabling the ANN to learn features such as device noise, operational disturbances, and other uncertainties common in practical systems.

4.1 Overcurrent Protection Verification

The overcurrent protection verification aims to examine the discrimination capability of protection thresholds during fault occurrences. Protection devices monitor real-time current via current transformers and compare it with preset thresholds; a trip signal is triggered when the current exceeds the threshold for a specified duration.

Under identical operating scenarios, a comparative analysis between fixed-threshold protection and the proposed artificial neural network-based adaptive threshold scheme reveals a quantifiable trade-off through statistical performance metrics. In the fixed threshold approach, increasing sensitivity by adopting a threshold multiplier of 1.1 significantly elevates the incidence of false operations, leading to a notable false trip tendency during load transients. Conversely, emphasizing selectivity through a higher threshold multiplier of 1.5 results in an increased failure to trip tendency, corresponding to hazardously sluggish response times when faults are characterized by rapid current rise. The adaptive scheme achieves a superior balance, sustaining a low false trip tendency while markedly improving fault detection capability, as evidenced by a reduction in the failure to trip tendency.

Figs. 7 and 8 illustrate the overcurrent protection response to a fault. During normal operation, the system current remains near its rated value. A protection device monitors this current via a current transformer. A processor continuously compares the measured current to a preset threshold. As long as the current is below this threshold, no trip is triggered, ensuring a reliable power supply.

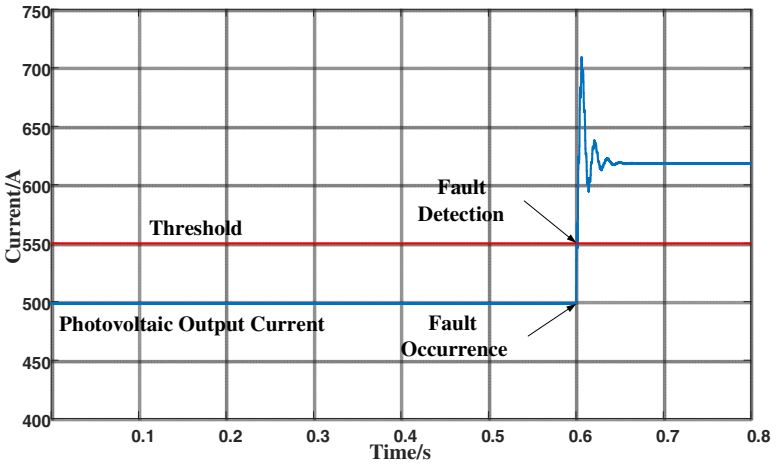

Figure 7: Detection at the photovoltaic output.

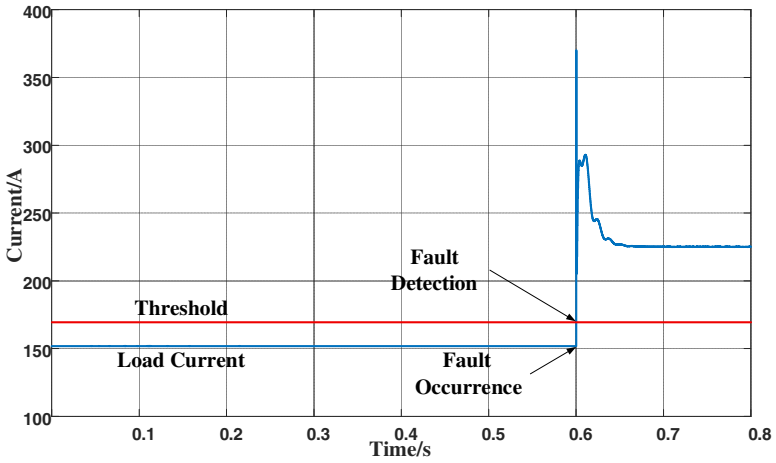

Figure 8: Detection at the load output.

Fig. 7 shows the overcurrent protection at the PV output. The red line indicates the protection threshold, while the blue waveform is the real-time PV current. Before a fault occurs, the current stays below the threshold, ensuring stable operation. At t = 0.6 s, a fault causes the current to surge to 700 A, exceeding the 550 A threshold. The protection system detects this and triggers the correct response. Fig. 8 displays the overcurrent protection result on the load side. Here, the red curve is the threshold, and the blue curve represents the load current. Prior to 0.6 s, the current remains around 150 A, below the 170 A threshold, so no protection acts. After the fault at 0.6 s, the current rises above 170 A, allowing the system to reliably detect and respond to the fault.

However, scenarios without threshold adjustment reveal the limitations of conventional methods. Fig. 9 illustrates the fault response process after a change in PV output without threshold adjustment. Between 0.3 and 0.5 s in Fig. 9, the change in PV output causes the line current to rise and exceed the protection threshold. However, the actual fault does not occur until 0.6 s. Therefore, without threshold adjustment, the fault cannot be accurately identified. This highlights the threshold matching problem in existing protection schemes when responding to PV output variations, specifically, that the protection setting does not account for current changes caused by PV power fluctuations.

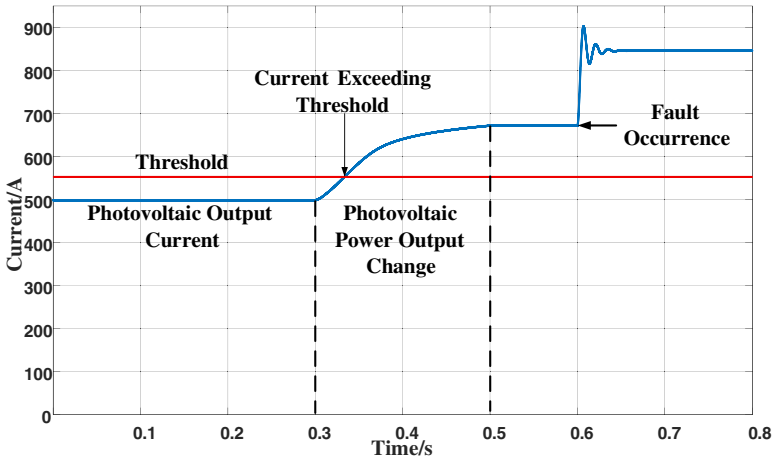

Figure 9: Protection configuration for photovoltaic output variation without threshold adjusting.

In summary, this verification demonstrates that while overcurrent protection with fixed thresholds can handle simple faults, it is susceptible to interference from operational events. The dynamic threshold optimization approach introduced in the proposed methodology is essential for improving reliability and establishes an empirical basis for the adaptive protection strategy.

4.2 Threshold Adaptive Setting

Theoretical analysis reveals that with the increase in PV penetration, the fault characteristics of distribution networks change significantly, and traditional fixed-threshold protection strategies struggle to adapt to the dynamic fluctuations of current distribution. The connection of PV power sources not only alters the magnitude and direction of fault currents but also introduces bidirectional power flow issues, which may lead to misoperation or refusal of protection devices, thereby threatening grid security. The efficacy of the proposed methodology is comprehensively demonstrated via experimental case studies under varying operational conditions.

To further validate the impact of varying PV penetration on the adaptive protection strategy, three comparative experimental scenarios were designed, as shown in Figs. 10–12. The red curve represents the dynamically adjusted protection threshold, and the blue curve corresponds to the PV output current. In the 0–0.3 s interval, the PV system is in normal operation, and the protection device is not triggered. When the PV output increases during the 0.3–0.5 s interval, the system detects the step change in current in real-time, triggering the adaptive threshold adjustment mechanism. In the low-ratio PV power generation scenario of Fig. 10, the threshold increases from 290 to 380 A between 0.3 and 0.5 s, ensuring that effective fault isolation capability is maintained even under power fluctuation conditions. When the fault occurs at 0.6 s, the line current instantly exceeds the protection threshold, and the threshold adjustment is halted. Similarly, in the moderate-ratio PV scenario (Fig. 11) and the high-ratio PV scenario (Fig. 12), the threshold is also dynamically adjusted between 0.3 and 0.5 s and stops adjusting when the fault occurs at 0.6 s.

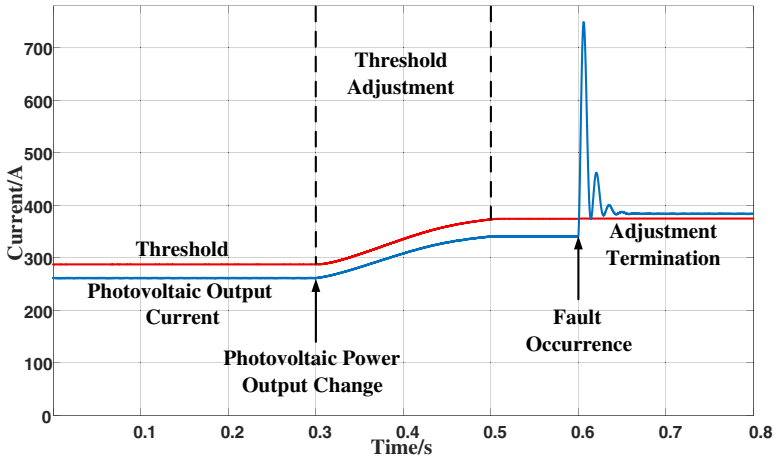

Figure 10: Threshold adjusting in low-ratio PV power systems.

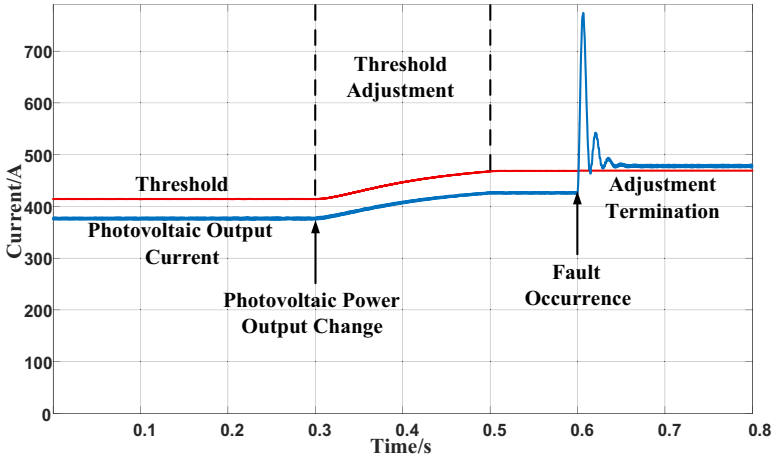

Figure 11: Threshold adjusting in moderate-ratio PV power systems.

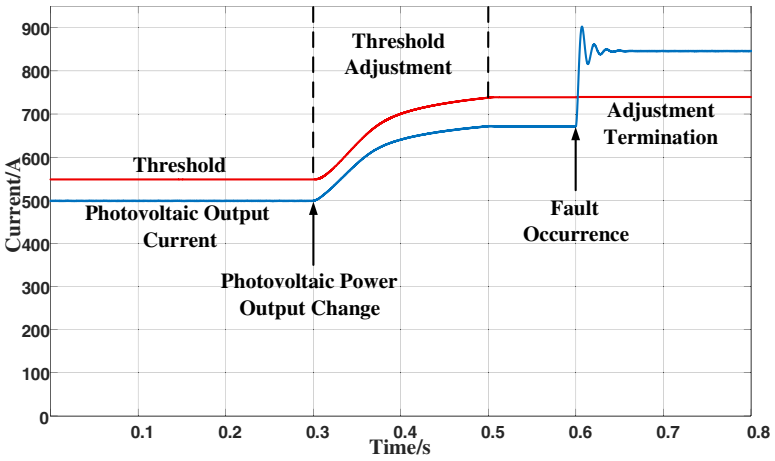

Figure 12: Threshold adjusting in high-ratio PV power systems.

Beyond validating the impact of PV penetration variations, it is equally critical to assess the robustness of the proposed adaptive protection strategy against fluctuations originating from the load side. Load variations, including sudden changes such as load shedding or connection/disconnection events, represent another significant source of dynamic disturbances in distribution networks. These load-induced current shifts can similarly challenge the stability and accuracy of fixed-threshold protection schemes.

To further validate the influence of different load variations on the adaptive protection strategy, another set of three comparative experiments was designed. Fig. 13 shows the threshold adjustment for a load shedding scenario under high-load conditions, Fig. 14 under moderate-load conditions, and Fig. 15 under high-load conditions. The red curve represents the dynamic protection threshold, and the blue curve is the load current waveform. In the 0–0.3 s interval, the load is in normal operation, and the protection device is not triggered. At 0.3 s, a load shedding operation occurs, triggering the dynamic threshold adjustment mechanism during the 0.3–0.5 s interval.

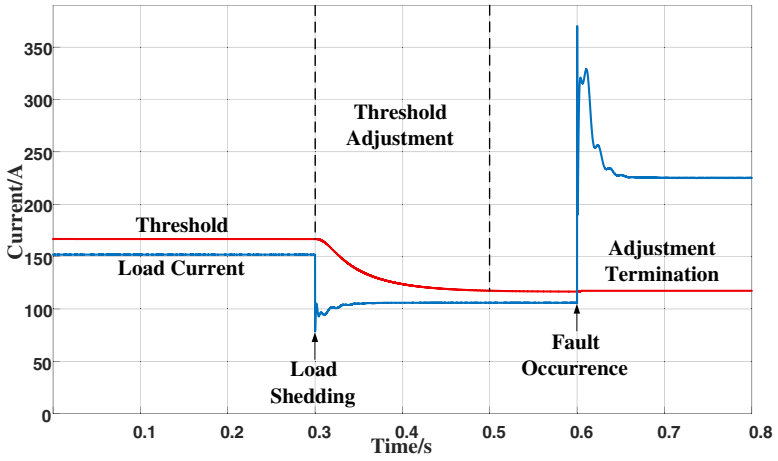

Figure 13: Threshold adjustment for load shedding under high-load conditions.

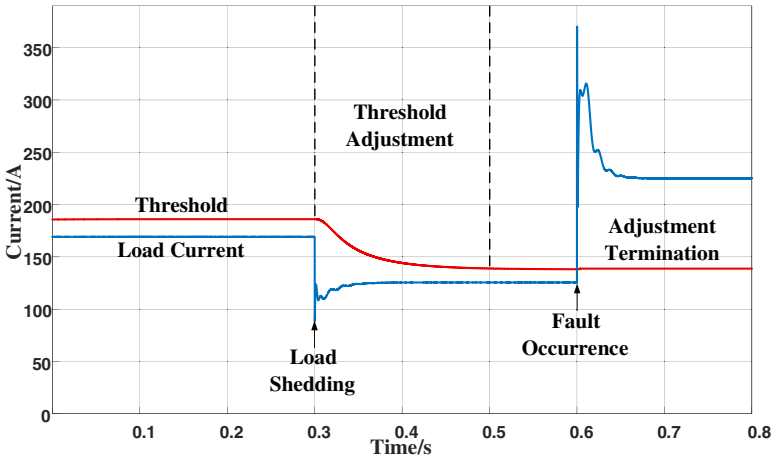

Figure 14: Threshold adjustment for load shedding under moderate-load conditions.

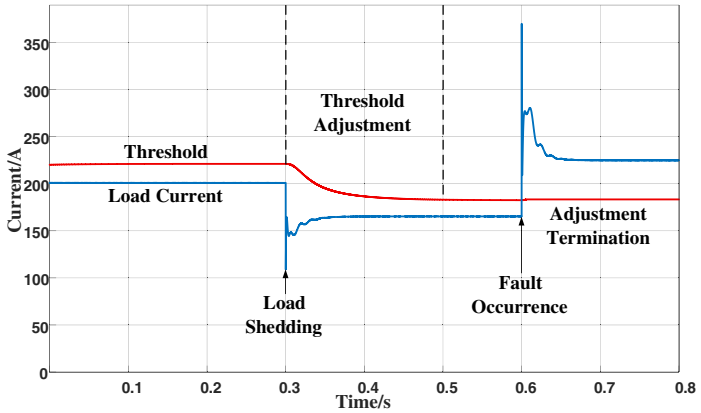

Figure 15: Threshold adjustment for load shedding under low-load conditions.

As shown in Fig. 13, the threshold current is adjusted from 170 to 130 A. At 0.6 s, a line fault occurs, the line current instantly exceeds the protection threshold, and the threshold is no longer adjusted. Similarly, in the load shedding scenario under moderate-load conditions (Fig. 14) and the high-load conditions (Fig. 15), the threshold is also dynamically adjusted between 0.3 and 0.5 s and stops adjusting when the fault occurs at 0.6 s. From the threshold adjustment trajectories described above, it can be observed that the adaptive mechanism of dynamic threshold adjustment maintains reliable operation during both PV ratio variations and load shedding operations. It also successfully terminates the threshold adjustment once the fault current exceeds the threshold.

The robustness of the proposed protection algorithm against measurement noise is ensured at both the data and decision-making levels. During dataset generation, random measurement noise and sensor errors are deliberately superimposed on current and voltage measurements. Specifically, Gaussian white noise with a signal-to-noise ratio (SNR) of 40 dB is added to the training data. Based on Fig. 13, the newly added Fig. 16 illustrates that the blue curve represents the original signal with noise, while the red curve denotes the stable threshold output by the ANN. The red curve shows no significant variation, because the algorithm takes the average value over a period of time; thus, it is capable of learning and extracting robust features even in the presence of signal interference. Regarding data latency, the proposed scheme is fully implemented on edge computing devices, eliminating communication delays associated with centralized architectures. Threshold updates and protection logic rely solely on local measurements, ensuring deterministic and bounded processing delays. In current relay protection practice, the maximum permissible error of current transformers is within ±10%. Errors within this range have relatively minor impact on the present study.

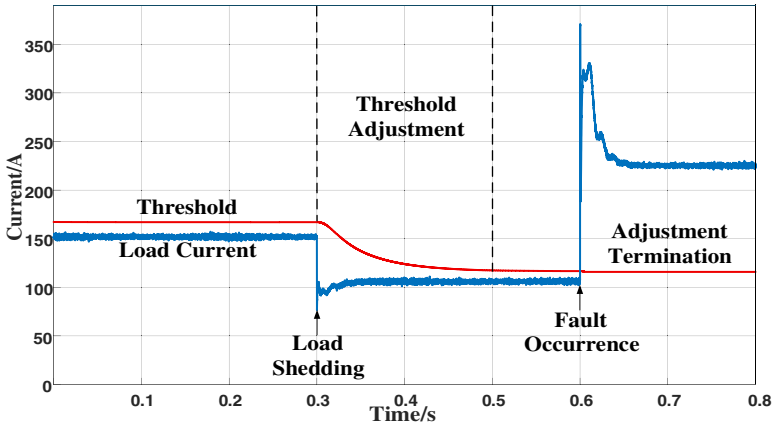

Figure 16: Threshold adjustment for load shedding under high-load conditions.

The neural network architecture adopted in this paper, a single hidden layer with 10 neurons, demonstrated exceptional performance in the experiments. Specifically, a simplified single-neural-network structure was validated as the most effective in a comparative analysis of Mean Absolute Error (MAE). The performance analysis bar chart in Fig. 17 clearly shows that the MAE value of this architecture is significantly lower than other comparative schemes, directly reflecting its high precision and low error characteristics in threshold prediction.

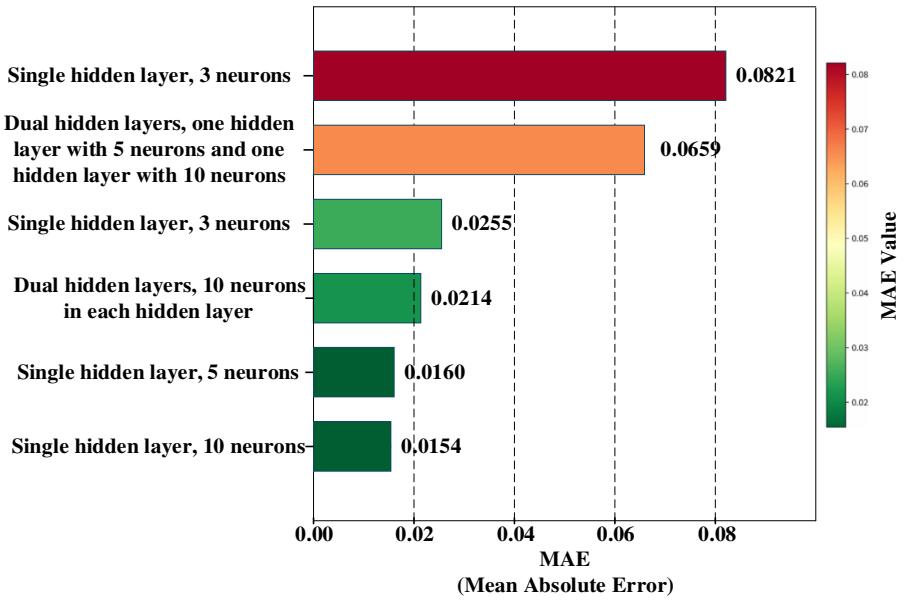

Figure 17: Comparative analysis of MAE performance across different neural network architectures.

During the adaptive threshold adjustment process, a low MAE value ensures that the protection system can accurately distinguish between normal fluctuations and fault currents, thereby reducing the risk of maloperations and enhancing overall reliability. Furthermore, compared to more complex networks, the architecture used in this paper offers superior computational efficiency, making it suitable for LVDC grid protection scenarios with high real-time requirements. Therefore, this architecture was established as the optimal choice, providing a solid data foundation for the practical application of the adaptive protection algorithm.

In Table 1 below, the performance indicators of three DC grid protection methods are systematically compared: the proposed ANN-based adaptive method, an adaptive Particle Swarm Optimization (PSO) method, and the traditional fixed-threshold method. This comparison aims to validate the superiority of the proposed algorithm in terms of false trip rate, failure-to-trip rate, and detection time. The specific data show that the proposed method's false trip rate is significantly lower than both the adaptive PSO and traditional methods, indicating its effectiveness in avoiding misjudgments caused by PV power fluctuations or load switching. In terms of the failure-to-trip rate, the proposed method is also the lowest, highlighting the precision of its dynamic threshold mechanism in distinguishing between faults and normal transients. Regarding detection time, the proposed method requires only 10 ms, outperforming the adaptive PSO and traditional methods, which confirms its rapid response capability.

Table 1: Performance comparison of different methods.

Index	Proposed Method	Adaptive PSO Method	Traditional Method
False Trip Rate (%)	1.05	1.7	8.2
Failure-to-Trip Rate (%)	1.52	2.3	12.5
Detection Time (ms)	10	12	20

These results collectively indicate that the proposed method, by dynamically optimizing thresholds via an ANN, provides robust data support for the reliable protection of low-voltage PV-energy storage DC distribution systems, highlighting its practical value in the energy management of zero-carbon parks.

Despite its effectiveness, the proposed ANN-based adaptive protection strategy has several limitations. Its performance depends on the representativeness of the training dataset. Although extensive operating scenarios, noise, and parameter uncertainties are included, extremely rare or previously unseen operating conditions may still affect prediction accuracy. Future work can pursue promising research directions and practical enhancements to strengthen the robustness and applicability of the proposed strategy. Incorporating online or transfer learning would enable incremental adaptation to new grid configurations or evolving operational patterns without full retraining. Embedding DC system dynamics into the ANN, potentially via physics-informed neural networks, can enhance interpretability and ensure that protection decisions remain consistent with domain constraints even under edge cases.

Based on the above, this paper makes the following contributions:

A dual-layer ANN architecture is proposed, mapping grid parameters to optimal protection thresholds.

A localized, dynamic threshold update mechanism is designed, which does not rely on high-speed communication and leverages edge computing for rapid response.

Extensive simulations validate the method's effectiveness and robustness under various operating conditions, including PV power fluctuations and load switching.

5 Conclusion

This study introduces a novel fault detection and protection algorithm for DC grids. The core innovation lies in replacing fixed protection thresholds with a dynamic threshold-setting strategy using ANNs, significantly improving reliability and adaptability. By leveraging local measurement data for ANN training, the algorithm eliminates the need for high-speed communication links. It effectively learns complex mappings between grid parameter variations—such as power fluctuations, load switching, and fault characteristics—to dynamically generate optimal protection thresholds across diverse operating conditions.

Simulations validate that the algorithm delivers rapid and accurate overcurrent protection while its adaptive threshold mechanism robustly handles operational changes, such as photovoltaic output surges and load shedding. This ensures reliable protection, preventing misoperations or failures under varying conditions. By relying on local data processing, the approach reduces implementation costs and mitigates communication delays, offering an effective solution for smarter, more robust LVDC grid protection.

Acknowledgement: Not applicable.

Funding Statement: This work is supported by the Key Science and Technology Project of China Southern Power Grid Co., Ltd. (GZKJXM20232507).

Author Contributions: The authors confirm contribution to the paper as follows: study conception and design: Zhukui Tan; data collection: Xiaoyong Cao, Qihui Feng; analysis and interpretation of results: Dong Liu, Xiayu Chen, Fei Chen; draft manuscript preparation: Zhukui Tan, Xiaoyong Cao. All authors reviewed and approved the final version of the manuscript.

Availability of Data and Materials: The data presented in this study are available on request from the corresponding author.

Ethics Approval: Not applicable.

Conflicts of Interest: The authors declare no conflicts of interest.

References

1. Suryadevara R, Parsa L. Full-bridge ZCS-converter-based high-gain modular DC-DC converter for PV integration with medium-voltage DC grids. IEEE Trans Energy Convers. 2019;34(1):302–12. doi:10.1109/TEC.2018.2878964.
2. Øgaard MB, Frimannslund I, Riise HN, Selj J. Snow loss modeling for roof mounted photovoltaic systems: improving the Marion snow loss model. IEEE J Photovolt. 2022;12(4):1005–13. doi:10.1109/JPHOTOV.2022.3166909.
3. Lee J, Kang J, Lee S, Oh HM. Ultra-short term photovoltaic generation forecasting based on data decomposition and customized hybrid model architecture. IEEE Access. 2024;12:20840–53. doi:10.1109/ACCESS.2024.3362234.
4. Ban GB, Tan ZK, Xu YT, Hao ZH, Yuan XF, Xu T. Research on topology structure of urban DC distribution engineering. Power Syst Big Data. 2019;22(9):1–7. (In Chinese). doi:10.19317/j.cnki.1008-083x.2019.09.001.
5. Chacko RLJ, Eapen RR, Sankar V. A study on LVDC systems for commercial building applications. In: Proceedings of the 2022 IEEE 19th India Council International Conference (INDICON); 2022 Nov 24–26. Kochi, India. p. 1–6. doi:10.1109/INDICON56171.2022.10039905.
6. Wang Y, Fan R, Fang G, Li L, Li J, Liu M. A method of distance protection setting calculation for AC/DC hybrid receiving-end power grid. In: Proceedings of the 2018 2nd IEEE Conference on Energy Internet and Energy System Integration (EI2); 2018 Oct 20–22. Beijing, China. p. 1–5. doi:10.1109/EI2.2018.8582250.
7. Saxena A, Sharma NK, Samantaray SR. An enhanced differential protection scheme for LVDC microgrid. IEEE J Emerge Sel Topics Power Electron. 2022;10(2):2114–25. doi:10.1109/jestpe.2022.3144300.
8. Wang D, Hu P, Cao Y, Syed M. A centralized post-transient derivatives based protection scheme for LVDC distribution networks. IEEE Trans Power Deliv. 2025;40(2):705–17. doi:10.1109/TPWRD.2024.3520244.
9. Buscariolli L, dos Santos RC, Pavani APG. New ANN-based method for islanding detection in distribution systems with PV generation. In: Proceedings of the 2023 IEEE PES Innovative Smart Grid Technologies Latin America (ISGT-LA); 2023 Nov 6–9; San Juan, PR, USA. p. 365–9. doi:10.1109/ISGT-LA56058.2023.10328216.
10. Mousavi A, Mousavi R, Mousavi Y, Tavasoli M, Arab A, Fekih A. Artificial neural networks-based fault localization in distributed generation integrated networks considering fault impedance. IEEE Access. 2024;12:82880–96. doi:10.1109/ACCESS.2024.3412991.
11. Wang S, Dehghanian P, Li L. Power grid online surveillance through PMU-embedded convolutional neural networks. IEEE Trans Ind Appl. 2020;56(2):1146–55. doi:10.1109/tia.2019.2958786.
12. Balati A, Li B, Chen Q, Cui D, Jiang J, Nan D. Analysis and control suggestions of transient characteristics of AC/DC hybrid power grid under DC faults. In: Proceedings of the 2021 IEEE International Conference on Advances in Electrical Engineering and Computer Applications (AEECA); 2021 Aug 27–28; Dalian, China. p. 224–32. doi:10.1109/aeeca52519.2021.9574399.
13. Bertho R, Lacerda VA, Monaro RM, Vieira JCM, Coury DV. Selective nonunit protection technique for multiterminal VSC-HVDC grids. IEEE Trans Power Deliv. 2018;33(5):2106–14. doi:10.1109/TPWRD.2017.2756831.
14. Vaidya D, Alam MN. Fault location in three terminal transmission lines using artificial neural networks. In: Proceedings of the 2025 13th International Conference on Smart Grid (icSmartGrid); 2025 May 27–29. Glasgow, UK. p. 583–6. doi:10.1109/icSmartGrid66138.2025.11071760.
15. Ankar S, Yadav A. ANN-based protection scheme for bipolar CSC-based HVDC transmission line. In: Proceedings of the 2019 Innovations in Power and Advanced Computing Technologies (i-PACT); 2019 Mar 22–23. Vellore, India; 2020. p. 1–5. doi:10.1109/i-PACT44901.2019.8960148.
16. Ghotbi-Maleki M, Azzouz MA, Sanaye-Pasand M. Resilience enhancement of adaptive overcurrent protection for active distribution networks against relay-setting cyber-attacks. IEEE Trans Ind Inform. 2025;21(11):9034–44. doi:10.1109/TII.2025.3594016.
17. Junjariya D, Tripathi JN. Large-scale optimization of decoupling capacitors using adaptive region based encoding scheme in particle swarm optimization. IEEE Open J Nanotechnol. 2022;3:210–9. doi:10.1109/OJNANO.2022.3224061.

18. Xia HY, Yang M, Luo JJ, Hong X, Xu W. LQT-based energy-efficient control for intelligent vehicles optimized by adaptive genetic algorithm. IEEE Access. 2025;13:96800–12. doi:10.1109/ACCESS.2025.3574217.
19. Luo B, Wu H, Wang M, Wang F, Bai L, Jiang C, et al. Front-end parameter identification method based on Adam-W optimization algorithm for underwater wireless power transfer system. IEEE Trans Power Electron. 2025;40(4):6307–18. doi:10.1109/TPEL.2024.3516493.
20. Shui PL, Zhang LX, Bai XH. Small target detection in sea clutter by weighted biased soft-margin SVM algorithm in feature spaces. IEEE Sens J. 2024;24(7):10419–33. doi:10.1109/jsen.2024.3350571.
21. Liu JH, Chen CC. Data-driven island detection using Chi-squared discretization-based random forest approach for microgrid with RES. IEEE Trans Ind Appl. 2025;61(1):1475–87. doi:10.1109/tia.2024.3462686.
22. Alhanaf AS, Farsadi M, Balik HH. Fault detection and classification in ring power system with DG penetration using hybrid CNN-LSTM. IEEE Access. 2024;12:59953–75. doi:10.1109/ACCESS.2024.3394166.